electronics

MDPI

Article

Model Predictive Control of Aero-Mechanical Actuators with Consideration of Gear Backlash and Friction Compensation

Qixuan Zuo [1], Bo Wang [2], Jingbo Chen [2] and Haiying Dong [1,*]

[1] College of New Energy and Power Engineering, Lanzhou Jiaotong University, Lanzhou 730070, China; 12222117@stu.lzjtu.edu.cn
[2] Lanzhou Wanli Airlines Electromechanical Limited Liability Company, Lanzhou 730070, China; wangb087@avic.com (B.W.); chenjb002@avic.com (J.C.)
* Correspondence: hydong@mail.lzjtu.cn

Abstract: To address the issues of low positional accuracy and significant torque pulsation caused by gear backlash and nonlinear friction in the mechanical transmission mechanism of aeronautical flap electromechanical actuators, we propose a model predictive control method for flap electromechanical actuator considering gear backlash and friction compensation. Firstly, we model the gear backlash in the electromechanical actuator's mechanical transmission mechanism and design a corresponding torque current compensation method using a simplified dead zone model. Secondly, the LuGre compensation friction model is introduced, and a friction torque current compensation method is developed to address the nonlinear friction torque generated during system operation. Finally, the proposed current compensation strategies are employed to mitigate the adverse effects of gear backlash and nonlinear friction on system control performance. The simulation results demonstrate that the proposed method enhances position tracking accuracy, reduces torque pulsation, and significantly improves the overall control performance of the system.

Keywords: electromechanical actuator; PMSM; gap deadband model; LuGre friction model; model predictive control

Citation: Zuo, Q.; Wang, B.; Chen, J.; Dong, H. Model Predictive Control of Aero-Mechanical Actuators with Consideration of Gear Backlash and Friction Compensation. *Electronics* **2024**, *13*, 4021. https://doi.org/10.3390/electronics13204021

Academic Editors: William Ditto and Roald M. Tiggelaar

Received: 15 July 2024
Revised: 5 September 2024
Accepted: 11 October 2024
Published: 12 October 2024

1. Introduction

With the rapid development of multi-electric aircraft, high-power-density electromechanical actuators (EMAs) have been widely promoted and applied in aircraft flight control systems [1]. Permanent magnet synchronous motors (PMSMs) are widely used as drive motors for EMAs due to their excellent starting performance, wide speed range, compact size, and light weight [2]. In the flap EMA of an aircraft high-lift system, the drive motor's position control requires high accuracy and disturbance resistance, while the flap EMA is a nonlinear, multi-variable system. During system operation, the gear backlash in the mechanical transmission mechanism, along with the reciprocating motion caused by dynamic and static friction, significantly impacts the speed and position control accuracy of the motor drive [3]. In electric servo systems with high precision requirements, the effects of gear backlash and friction are critical and cannot be overlooked. Therefore, it is crucial to investigate the impact of these factors on flap EMAs, as they significantly contribute to the degradation of the system's control performance.

Gear backlash frequently occurs between transmission mechanisms and is a common nonlinear disturbance in industrial processes. It is also a significant nonlinear characteristic that affects the performance metrics of servo systems. Gear backlash compensation can be approached both mechanically and through control algorithms. Mechanical solutions, such as using dual motor drives or adding spring devices, can eliminate gaps but are often inefficient and increase equipment cost and weight. In contrast, control algorithm-based compensation avoids these mechanical drawbacks. Common methods of gap compensation include inverse gap compensation, observer compensation, etc. Inverse backlash compensation uses a gear

backlash model to create an inverse model, which is then converted into a control quantity that is added to the system's control signal to counteract the backlash nonlinearity [4]. The authors of reference [5] developed a discrete adaptive inverse gap controller capable of rapidly determining gap parameters. However, this method exhibits discontinuities in the inverse gap compensation characteristics, which can lead to vibration issues. When using an observer for gap compensation, the gap is treated as an external disturbance. The designed observer can monitor the gap disturbance term in real time, allowing for the development of a corresponding feedforward compensation strategy based on the observed disturbance [6,7]. In reference [8], current and speed controllers are integrated into a single-loop model predictive controller for a permanent magnet synchronous motor system, utilizing a holistic approach to address external disturbances. However, this integral compensation often compromises the system's dynamic performance. The disturbance observer is highly sensitive to the initial conditions of the system; deviations from these initial conditions can impair its ability to accurately estimate system disturbances [9]. Additionally, the observer's performance is strongly dependent on an accurate mathematical model of the controlled object. Inaccuracies in the model or significant variations in system parameters can substantially affect the observer's performance, leading to ineffective compensation [10].

In terms of control methods, traditional linear control algorithms often struggle to achieve optimal control performance, especially when addressing dynamic response and interference immunity. To meet these requirements, many nonlinear algorithms such as sliding mode control [11], robust control [12], fuzzy control [13], adaptive control [14], active disturbance rejection control [15,16], and model predictive control [17] can be used for research into gear backlash. A key characteristic of backlash nonlinearity is its generation of variable gear torque. While the integral term in PID control is effective at suppressing constant-value perturbations, it has limitations in addressing time-varying disturbances. Reference [11] proposes a terminal sliding mode controller to address the backlash problem in electromechanical actuating systems. This approach uses a continuously differentiable function to approximate the backlash model, treats the model discrepancy as an external aggregate disturbance, establishes a state-space model of the system with respect to this disturbance, and designs the terminal sliding mode controller to compensate for the backlash. Reference [12] views the tooth gap model as a globalized linear model in which there is a bounded modeling error due to the non-intersection of different linear parts. An adaptive robust controller is designed based on this model, effectively addressing the backlash nonlinearity and significantly improving the system's speed tracking accuracy. Reference [13] proposes a fuzzy adaptive sliding mode control method for asymptotic trajectory tracking of robotic manipulators with control gap and uncertainty. A fuzzy logic system is introduced into the sliding mode control to estimate the uncertainty of the system, to compensate for unknown concentrated disturbances and to accelerate the convergence process. Reference [14] proposes an adaptive neural control method for a class of non-strict-feedback stochastic nonlinear systems with unknown backlash hysteresis. This method ensures that all signals in the closed-loop system remain semi-globally consistent and ultimately bounded in the fourth-moment sense, and that the tracking error converges to a small neighborhood of the origin. Reference [16] employs a self-imposed perturbation control strategy by treating the backlash nonlinearity as an external disturbance. It considers both the external perturbation and internal uncertainties as dilation states, and designs a dilation state observer to monitor and compensate for them. This approach significantly enhances the system's dynamic performance.

To mitigate the effects of nonlinear friction on the servo system [18,19], researchers both domestically and internationally have employed control compensation techniques to counteract the frictional torque. Currently, the widely used classical friction models are mainly the following: the Coulomb–viscous friction model [20], Stribeck model [21], Dahl model [22], LuGre model [23], and so on. Among them, the LuGre friction model is commonly used in typical servo systems for compensation, which utilizes the relevant theoretical foundations of the Dahl model and the bristle model, fully reflects the friction motion mechanism, portrays all

the nonlinear characteristic effects of friction, and has been widely used in servo systems [24]. The literature [25] introduces an extended LuGre friction model aimed at estimating dynamic and position-dependent friction effects, specifically to capture the nonlinear friction characteristics of long-stroke machine tool axis systems. Reference [26] investigated frictional effects in a lubricated linear roller guideway system, addressing both pre-slip and slip zones. The experimental measurements demonstrated that this modified LuGre model accurately predicted the dynamic behavior of the frictional contact interface.

In summary, to address the issue of control accuracy degradation caused by gear backlash and nonlinear friction in the mechanical transmission mechanism of aeronautical flap electromechanical actuators, this paper proposes an aeronautical electromechanical actuator model predictive control method considering clearance and friction compensation, which effectively integrates the gear backlash compensation with the friction compensation to improve the control accuracy. Specifically, a deadband-based gear backlash compensation model is selected, which accounts for both the damping and rigidity characteristics of the gears, while accurately describing the dynamic relationship between gear torque and the relative position of the master and slave gears. At the same time, the LuGre friction model is used to deal with the friction compensation problem. The LuGre model is able to fully reflect the motion mechanism of friction and accurately represents all the nonlinear characteristics of friction with its unique advantages. By combining these two models, the proposed approach can more accurately simulate the gear characteristics under real working conditions. Based on this, a compensation strategy for the gear gap torque current and friction torque current is designed using the deadband compensation model and LuGre friction model, and the control law is redesigned. The feedforward compensation method combined with model predictive control is used to accurately compensate and control the q-axis current of the system, which significantly enhances the overall system performance. Finally, the method proposed in this paper is verified by building a MATLAB/Simulink simulation model, and the simulation results show that the method proposed in this paper has obvious advantages in effectiveness and feasibility.

2. Modeling of Aeronautical Flap Electromechanical Actuation Systems

Figure 1 presents a schematic diagram of the electromechanical actuator, which consists of a flight control computer, an actuator control unit, a power supply, a permanent magnet synchronous motor (PMSM), a reducer, and a roller screw. The system operates as follows: the flight control computer sends a position command, which is then processed by the actuator control unit. This unit collects position feedback from the PMSM and the linear displacement data from the linear variable differential transformer (LVDT). It performs highly dynamic closed-loop control of position and speed by coordinating the motor-driven gearbox, roller screw, and other components, thereby enabling the flaps to execute the lowering and retracting actions [27].

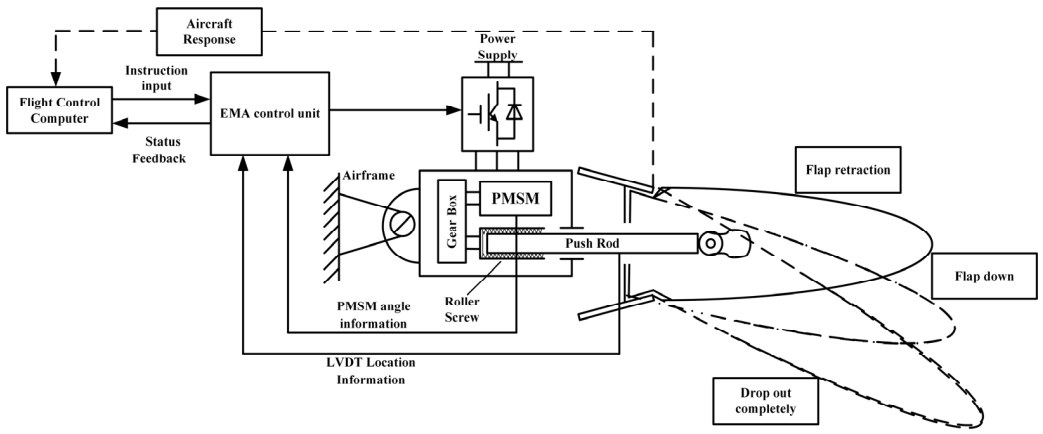

Figure 1. Structure of flap electromechanical actuator.

2.1. Permanent Magnet Synchronous Motor Modeling

The equation of state of the surface-mounted permanent magnet synchronous motors in the synchronized rotating coordinate system is

$$\frac{di_{\mathrm{d}}}{dt} = \frac{1}{L_{\mathrm{s}}}(-R_{\mathrm{s}}i_{\mathrm{d}} + \omega_{\mathrm{e}}L_{\mathrm{s}}i_{\mathrm{q}} + u_{\mathrm{d}}) \tag{1}$$

$$\frac{di_{\mathrm{q}}}{dt} = \frac{1}{L_{\mathrm{s}}}(-R_{\mathrm{s}}i_{\mathrm{q}} - \omega_{\mathrm{e}}L_{\mathrm{s}}i_{\mathrm{d}} - \omega_{\mathrm{e}}\psi_{\mathrm{f}} + u_{\mathrm{q}}) \tag{2}$$

$$T_{\mathrm{e}} = \frac{3}{2}P_{\mathrm{n}}\psi_{\mathrm{f}}i_{\mathrm{q}} \tag{3}$$

$$J\frac{d\omega_{\mathrm{m}}}{dt} = T_{\mathrm{e}} - T_{\mathrm{L}} - B\omega_{\mathrm{m}} \tag{4}$$

$$\omega_{\mathrm{e}} = P_{\mathrm{n}} \cdot \omega_{\mathrm{m}} \tag{5}$$

where R_{s} is the stator resistance; u_{d} and u_{q} are the voltage components of the d-axis and q-axis, respectively; i_{d} and i_{q} are the current components of the d-axis and q-axis, respectively; ω_{e} is the electrical angular velocity of the permanent magnet synchronous motors; ω_{m} is the mechanical angular velocity of the permanent magnet synchronous motors; Ψ_{f} is the magnetic chain of the permanent magnet; T_{e} is the electromagnetic torque; T_{L} is the load torque; P_{n} is the number of pole pairs of the motor; J is the inertia; and B is the coefficient of viscous friction, tabulated as the d-q-axis inductance of the surface-mounted permanent magnet synchronous motors being equal, i.e., $L_{\mathrm{d}} = L_{\mathrm{q}} = L_{\mathrm{s}}$.

2.2. Modeling of Mechanical Drive Systems

The EMA mechanical drive mechanism primarily consists of gearboxes, clutches, roller screws, and a push rod. In this system, the motor-driven gearbox converts rotary motion into linear motion through the roller screw, which drives the mechanical load to the desired position. In the simulation model, the mechanical drive system is divided into four components: the gear reduction box, the roller screw, gear backlash, and friction interference. The first two components connect the output speed of the PMSM with proportional and integral control to represent the gear reduction ratio and the rotary motion generated by the roller screw. The gear backlash is modeled using a clearance model, and then the system linear displacement x can be expressed as

$$x = \frac{\theta_{\mathrm{d}}L}{2\pi} \tag{6}$$

where θ_{d} is the rotation angle of the gearbox-driven wheel; and L is the lead of the roller screw.

The mathematical model of gear backlash can be described as

$$\tau(t) = \begin{cases} k(\Delta\theta(t) + \alpha) + c\dot{\Delta\theta}(t), \ \Delta\theta(t) \le -\alpha \\ 0 \qquad\qquad\quad , |\Delta\theta(t)| < \alpha \\ k(\Delta\theta(t) - \alpha) + c\dot{\Delta\theta}(t), \ \Delta\theta(t) \ge \alpha \end{cases} \tag{7}$$

$$\Delta\theta = \theta_{\mathrm{m}} - \frac{1}{m} \cdot \theta_{\mathrm{d}} \tag{8}$$

where τ is the torque between the gear sets, k and c are the stiffness coefficients and damping coefficients of the gears, respectively; θ_{m} and θ_{d} are the current positions of the master and the slave wheels; α is the deadband range; $\Delta\theta$ is the gear backlash error; and m is the gear ratio.

2.3. EMA Load Model

The mechanical transmission system drives the flap load in a linear motion, which is typically modeled as a classic spring–mass–damper system. The equivalent dynamic model is shown in Figure 2 [28].

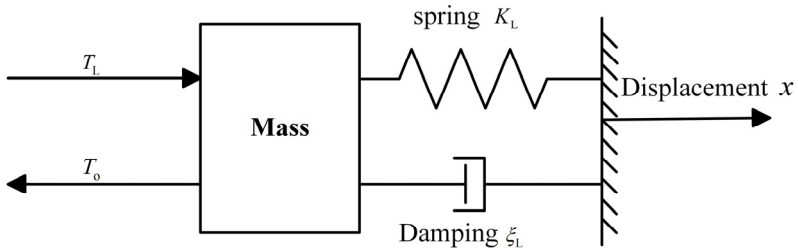

Figure 2. Dynamic model after load simplification.

According to the spring–mass–damping model after equivalence,

$$T_L(t) = T_o(t) + m_L \frac{d^2x(t)}{dt^2} + \xi_L \frac{dx(t)}{dt} + K_L x(t) \tag{9}$$

The Laplace transform gives

$$T_L(s) = T_o(s) + (m_L s^2 + \xi_L s + K_L)x(s) \tag{10}$$

The transfer function with respect to load is

$$G_{T_L} = \frac{1}{m_L s^2 + \xi_L s + K_L} \tag{11}$$

Here, T_L denotes the driving torque required by the equivalent model, T_o represents the torque from nonlinear factors caused by other disturbances in the actual load, m_L indicates the mass of the mass block in the load-equivalent model, ξ_L is the damping coefficient, K_L is the elasticity coefficient, and x represents the actual displacement of the load.

3. Model Predictive Control Considering Gap and Friction Compensation

The mechanical transmission mechanism of the aero flap electromechanical actuator is affected by various disturbance factors, such as gear backlash and nonlinear friction, which significantly impact system stability and position control accuracy. During flap EMA operation, the permanent magnet synchronous motor (PMSM) may experience variations in parameters and load perturbations, complicating the maintenance of optimal control performance in practical environments. To address these challenges, this paper designs a feedforward compensation strategy for gap and friction torque currents. This strategy incorporates a simplified deadband model for gap compensation and a LuGre friction compensation model to counteract system gaps and nonlinear friction. The objective is to eliminate nonlinear disturbances, achieve accurate system modeling, and enhance the control performance of the flap EMA. The overall structure of the control system is shown in Figure 3.

3.1. Gear Backlash Compensation Modeling

In flap electromechanical actuators, the gear action process involves two main aspects: instantaneous impacts caused by speed differences between the master and slave gears, and mutual extrusion resulting from positional discrepancies between these gears. The mutual gear torque between the gear sets is also influenced by these two factors. In the deadband model, the input signals are the speed difference $\Delta\omega(t)$ and the position difference $\Delta\theta$ between the master and slave gears, respectively, and the output is the torque between the

gear sets. In this model, we assume that the transmission is purely rigid, so the damping component is neglected in the modeling process, then the simplified gap dead zone model can be written as in the form of Equation (12).

$$\tau_c(t) = \begin{cases} k(\Delta\theta(t) + \alpha), \Delta\theta(t) \le -\alpha \\ 0 \quad , |\Delta\theta(t)| < \alpha \\ k(\Delta\theta(t) - \alpha), \Delta\theta(t) \ge \alpha \end{cases} \tag{12}$$

The simplified mathematical expression of the dead zone model mentioned above contains non-differentiable components, which can be corrected by introducing the Sigmoid function. The corrected dead zone model is presented in Equation (13).

$$\tau_c(t) = k\left(\Delta\theta(t) - \alpha\frac{1 - e^{-\frac{2}{\alpha}\Delta\theta(t)}}{1 + e^{-\frac{2}{\alpha}\Delta\theta(t)}}\right) \tag{13}$$

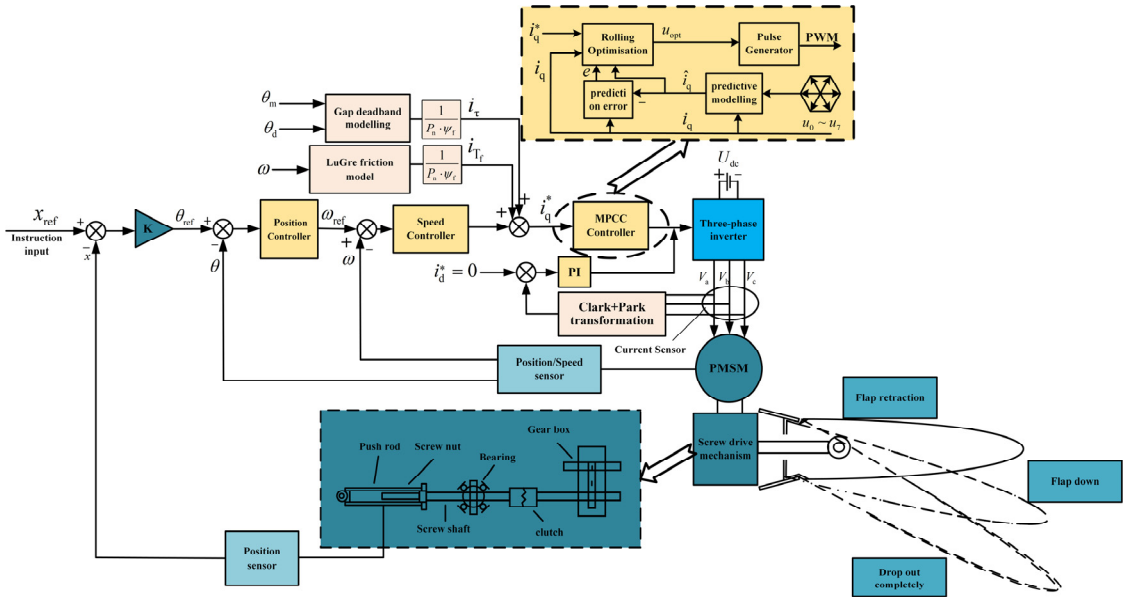

Figure 3. MPC control structure considering gap and friction compensation.

3.2. LuGre Friction Compensation Model

The nonlinear friction disturbance is described using the LuGre friction model, which represents the friction behavior through the contact, deformation, and generated relative displacement of elastic bristles [29]. The bristle structure of the model is illustrated in Figure 4.

Compared to traditional friction models, the LuGre friction model can comprehensively capture various static and dynamic friction phenomena. The specific mathematical model is as follows:

$$\frac{dz}{dt} = \omega + \frac{\sigma_0|\omega|}{g(\omega)}z \tag{14}$$

$$g(\omega) = \frac{F_c + (F_s - F_c)\exp[-(\frac{\omega}{\omega_s})^2]}{\sigma_0} \tag{15}$$

$$F_f = \sigma_0 z + \sigma_1\frac{dz}{dt} + \sigma_2\omega \tag{16}$$

where z is the bristle shape variable; ω is the relative velocity between contact surfaces; F_c is the Coulomb friction; F_s is the maximum static friction; F_f is the total friction of the mechanical drive system; σ_0 is the stiffness coefficient; σ_1 is the damping coefficient; σ_2 is the coefficient of viscous friction; and ω_s is the Stribeck velocity.

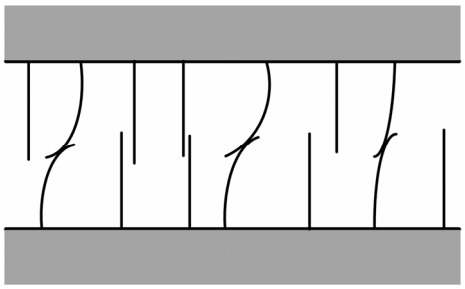

Figure 4. LuGre model bristle structure.

From the above equation, the friction model curve is shown in Figure 5.

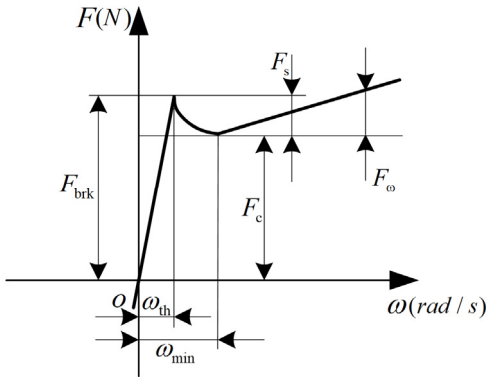

Figure 5. LuGre friction model curve.

In Figure 5, ω_{th} is the velocity threshold in the linear region; $\omega_{\min}$ is the minimum velocity required to transform static friction into viscous friction; F_{brk} is static friction; F_ω is viscous friction; F_c is the Coulomb friction; and F_s is the maximum static friction.

When the system is operating at a stable level $\frac{dz}{dt} = 0$, substituting it into Equation (14) yields

$$\frac{dz}{dt} = \omega + \frac{\sigma_0|\omega|}{g(\omega)}z = 0 \tag{17}$$

$$g(\omega) = z \cdot \text{sgn}(\omega) \tag{18}$$

Substituting Equation (18) into Equation (15) gives

$$\sigma_0 z = \left(F_c + (F_s - F_c)e^{-\left(\frac{\omega}{\omega_s}\right)^2}\right)\text{sgn}(\omega) \tag{19}$$

Substituting Equations (17) and (19) into Equation (16) gives

$$F_f = \left(F_c + (F_s - F_c)e^{-\left(\frac{\omega}{\omega_s}\right)^2}\right)\text{sgn}(\omega) + \sigma_2\omega \tag{20}$$

3.3. Gap and Friction Compensation MPCC Controller Design

Gear backlash torque and friction torque, as external perturbations, not only cause steady-state fluctuations in system speed and reduce the system's steady-state accuracy but also induce torque pulsations, which degrade the accuracy of EMA position control. This limits the application of the electromechanical actuator in high-precision control scenarios. To improve the control performance of the electromechanical actuator, this paper proposes a current compensation strategy to address gear backlash torque and friction torque in the mechanical transmission mechanism. The strategy compensates for these disturbances by adjusting the electrical current. The compensation principle is illustrated in Figure 6.

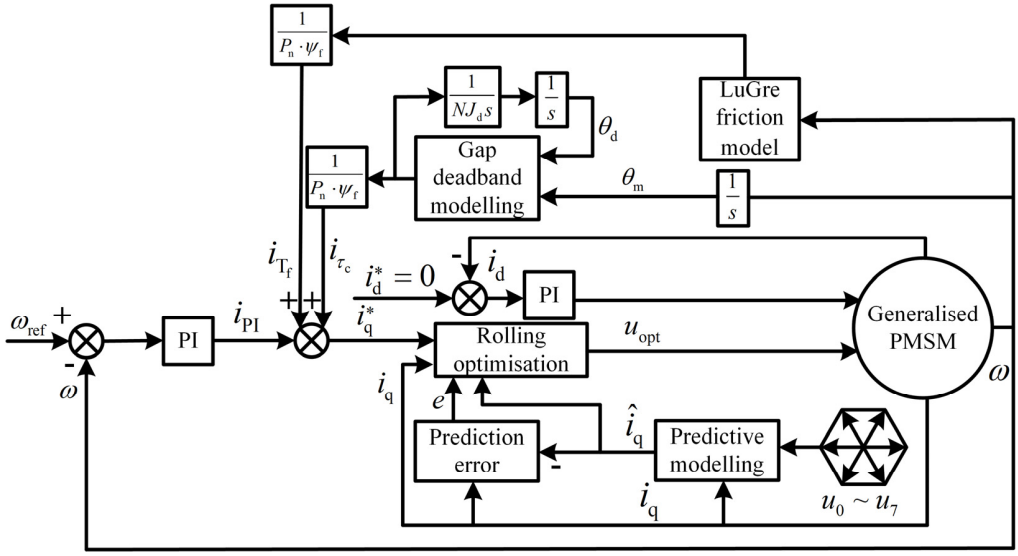

Figure 6. Schematic diagram of MPC based on gap and friction compensation.

In Figure 6, the system speed loop controller and current loop d-axis controller use PI controllers, while the q-axis current loop controller employs a model predictive controller. θ_m represents the position of the master wheel, θ_d represents the position of the driven wheel, the gap dead zone model is described by Equation (13), and the LuGre friction model is described by Equation (20). The effects of gear backlash torque and friction torque perturbations are compensated for in the form of electric current, with the compensation equation given by $i_q^* = i_{PI} + i_{Tf} + i_{\tau c}$. The control law consists of three components: i_{PI}, which is the PI control output; $i_{\tau c}$, which represents the current compensation based on the backlash model; and i_{Tf}, which represents the current compensation based on the friction model. The reference value i_q^* of the q-axis current, obtained from the speed loop, is then input to the q-axis controller.

The control process for predicting the q-axis current is as follows: by applying the optimal voltage vector $u_{opt}(k)$ determined at the $k-1$ control moment, the current $i_q(k)$, DC bus voltage, and rotational speed can be obtained at the k moment. Using the speed loop and current compensation from the backlash and friction models, the reference value for the q-axis current i_q^* can be obtained. The predicted current is calculated at $k+1$ moments under the action of $u_{opt}(k)$ according to Equation (23); in the actual system, the q-axis current $\hat{i}_q(k+1|k)$ is predicted at $k+1$ moments under the action of $u_{opt}(k)$. In the actual system, there is an error between the predicted value of q-axis current and the actual value. The prediction error is obtained by making a difference between the predicted value of q-axis current and the actual value at $k+1$ moments through Equation (27), and the predicted q-axis current at the next moment is corrected by Equation (28) using error weighting. Finally, the value function is used to judge the error of the current prediction value through Equation (29), the current prediction value that minimizes the total error of the q-axis current prediction is selected, and its corresponding switching state is output in the next cycle.

Since $i_d \equiv 0$ and the d-axis current controller is PI-controlled, only the q-axis current equation was studied. Defining T_s as the sampling period, the q-axis current state equation in Equation (2) is discretized at two adjacent sampling points k and $k+1$ using the first order Euler method as follows:

$$i_q(k) = \left(1 - \frac{R_s T_s}{L_s}\right) i_q(k-1) - \omega_e L_s T_s i_d(k-1) - \frac{\psi_f T_s}{L_s}\omega_e + \frac{T_s}{L_s} u_q(k-1) \tag{21}$$

$$i_q(k+1) = \left(1 - \frac{R_s T_s}{L_s}\right) i_q(k) - \omega_e L_s T_s i_d(k) - \frac{\psi_f T_s}{L_s}\omega_e + \frac{T_s}{L_s} u_q(k) \tag{22}$$

Since $i_d \equiv 0$, the coupling term about i_d in the above equation is not considered, and the difference between Equations (22) and (21) yields the predicted value of the q-axis current at the moment $k + 1$ as

$$\hat{i}_q(k+1|k) = \left(2 - \frac{R_s T_s}{L_s}\right) i_q(k) - \left(1 - \frac{R_s T_s}{L_s}\right) i_q(k-1) + \frac{T_s}{L_s} \Delta u_q(k) \tag{23}$$

where $\Delta u_q(k) = u_q(k) - u_q(k-1)$ is the voltage increment at moment k; when $C = 1 - R_s T_s / L_s$ and $D = T_s / L_s$, then Equation (23) can be simplified to

$$\hat{i}_q(k+1|k) = (C+1) i_q(k) - C i_q(k-1) + D \Delta u_q(k) \tag{24}$$

The predicted value of the q-axis current at the moment $k + 2$ can be called recursively from Equation (24)

$$\hat{i}_q(k+2|k) = \left(C^2 + C + 1\right) i_q(k) - (C^2 + C) i_q(k-1) + (C+2) D \Delta u_q(k) \tag{25}$$

The predicted value of the q-axis current at moment N is given by the generalized equation

$$\hat{i}_q(k+N|k) = \sum_{i=0}^{N} C^i i_q(k) - \sum_{j=1}^{N} C^j i_q(k-1) + \sum_{n=1}^{N-1} (N-n) C^n D \Delta u_q(k) \tag{26}$$

In the actual system, there is an error between the predicted value of the q-axis current and the actual value, the difference between the predicted value of the q-axis current at moment k and the actual value is obtained as the prediction error, and in order to facilitate the study, it is assumed that the prediction error at any moment is a fixed value, i.e.,

$$e(k+N) = e(k+N-1) = \ldots = e(k+1) = e(k) = i_q(k) - \hat{i}_q(k) \tag{27}$$

Correcting the predicted values of q-axis currents at other moments by error weighting yields the following:

$$\hat{i}'_q(k+N|k) = \hat{i}_q(k+N|k) + \delta e(k) \tag{28}$$

The three-phase two-level inverter has eight distinct switching states, each corresponding to a specific voltage vector. Utilizing the concept of finite-set model predictive control, the inverter's current prediction values for all switching states are evaluated. To ensure precise current tracking, a cost function is employed to assess the prediction error. The switching state that minimizes the total q-axis current prediction error is selected and applied in the next cycle. The value function is defined as follows.

$$\min J_{\mathrm{MPCC}} = \sum_{j=1}^{N_y} \left\| i_q^*(k+j|k) - \hat{i}'_q(k+j|k) \right\|^2 + \sum_{j=0}^{N_{u-1}} \left\| \Delta u_q(k+j|k) \right\|^2 \tag{29}$$

$$i_q^* = i_{\mathrm{PI}} + i_{\tau_c} + i_{T_f} \tag{30}$$

$$i_{\tau_c} = \frac{\tau_c}{P_n \cdot \psi_f} \tag{31}$$

$$i_{T_f} = \frac{F_f}{P_n \cdot \psi_f} \tag{32}$$

where N_y and N_u ($N_y \geq N_u \geq 1$) denote the prediction time domain and control time domain; i_{PI} is the output current of the speed loop PI controller; $i\tau_c$ is the gear backlash torque compensation current; i_{Tf} is the LuGre friction torque compensation current; and i_q* is the q-axis current reference value.

4. Simulation Verification and Results Analysis

In this paper, MATLAB/Simulink R2022a was used to build the system simulation model, and the PMSM parameters were set as shown in Table 1. The system sampling frequency was set to 10 kHz, and the total simulation time was 1 s.

Table 1. Parameters of permanent magnet synchronous motor.

Parameter	Value	Symbol/Unit
Stator resistance	2.875	R_s/Ω
Stator inductance	8.5	L_s/mH
Permanent magnet chain	0.09	Ψ_f/Wb
Moment of inertia	0.002	$J/(kg{\cdot}m^2)$
Motor pole pair number	4	-
Rated speed	1000	$\omega/(r/min)$
Inverter operating voltage	270	U_{dc}/V

Table 2. LuGre friction model parameter settings.

Parameter	σ_0	σ_1	σ_2	F_c/N	F_s/N	$\omega_s/r{\cdot}s^{-1}$
Value	83895.4	259.4842	27.8623	3.8145	8.1635	0.0124

Table 3. Gear backlash deadband model parameter settings.

Condition	$\Delta\theta > \alpha$		$\Delta\theta < -\alpha$	
Parameter	k	α	k	α
Value	586.9952	0.00301	565.0363	0.00314

To ensure a closer fit to real-world conditions and to better verify the effectiveness of the proposed compensation control method, this study refers to the data obtained from the experimental research in references [30,31] to set the parameters of the gear backlash model and the friction compensation model. The specific parameters are provided in Tables 2 and 3. Based on this, this study compares the traditional PI control method, the MPCC method, and the PI control method (Compensate–PI) with the MPCC method (Compensate–MPCC) after the flap EMA is compensated for the gap and friction; the simulation results are shown in Figures 7–14, and the data comparisons are shown in Tables 4–7.

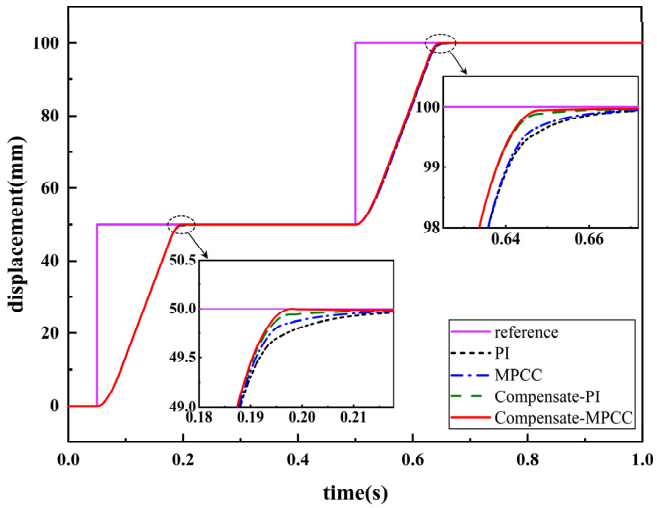

Figure 7. Output displacement tracking graph for inverter operating voltage.

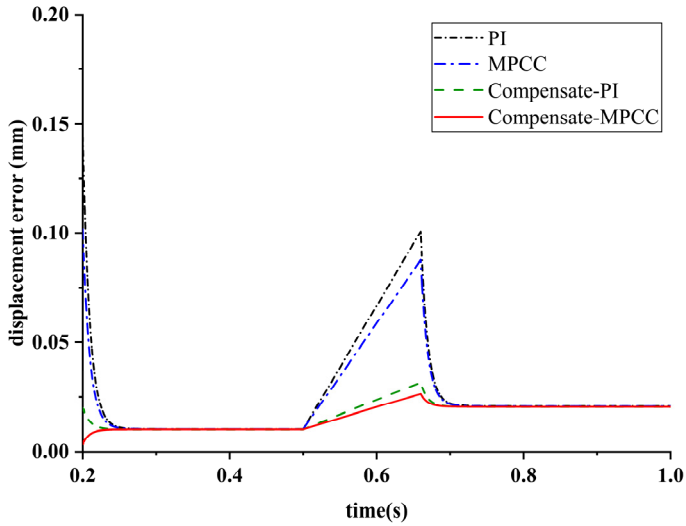

Figure 8. Position error graph.

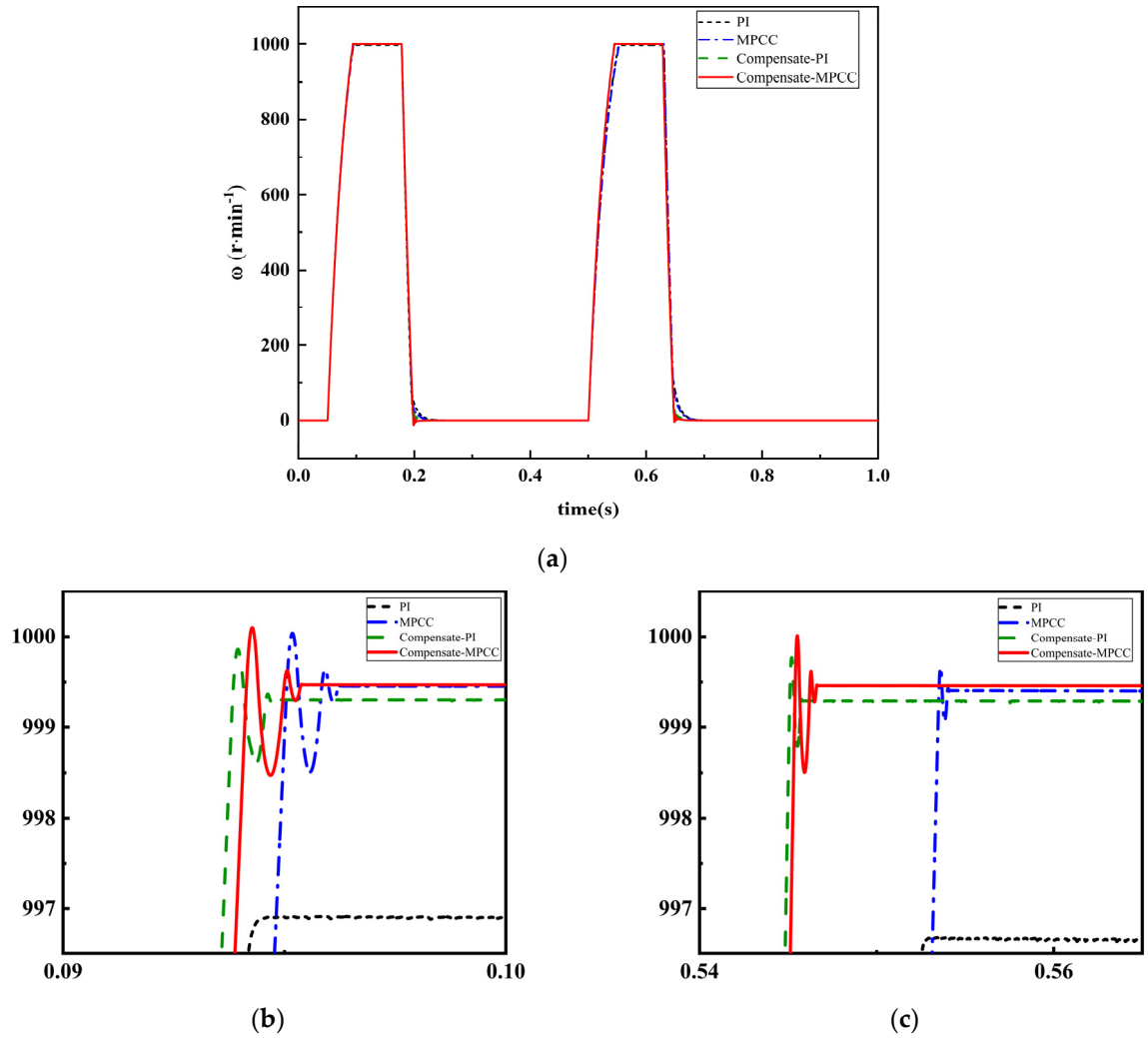

Figure 9. Speed graphs. (**a**) General curve of speed. (**b**) Partial enlargement 1. (**c**) Partial enlargement 2.

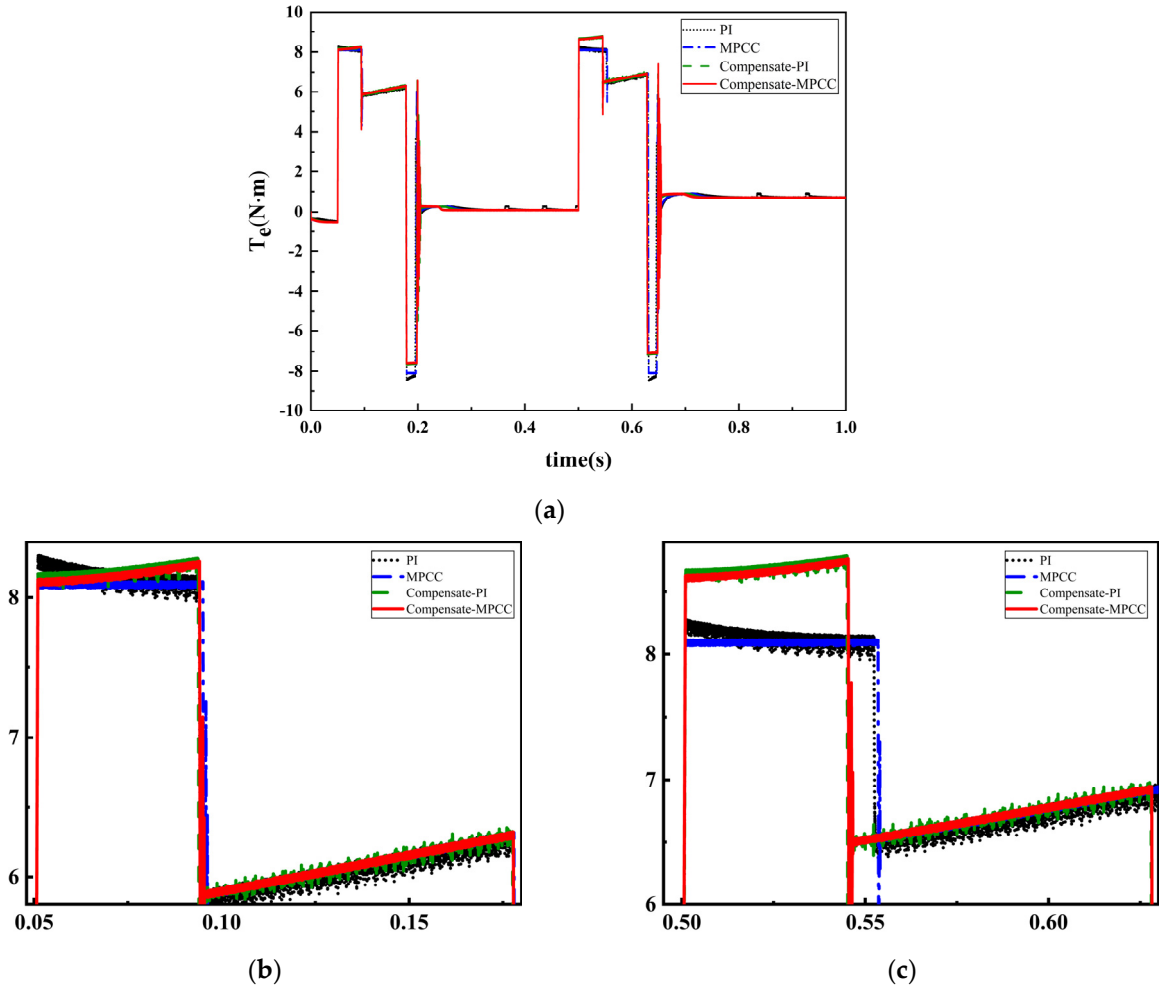

Figure 10. Electromagnetic torque graphs. (**a**) General curve of electromagnetic torque. (**b**) Partial enlargement 1. (**c**) Partial enlargement 2.

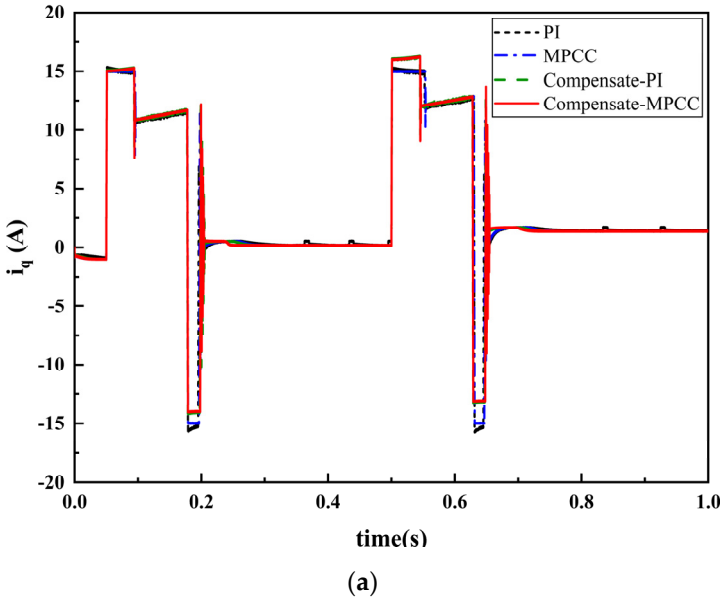

Figure 11. *Cont.*

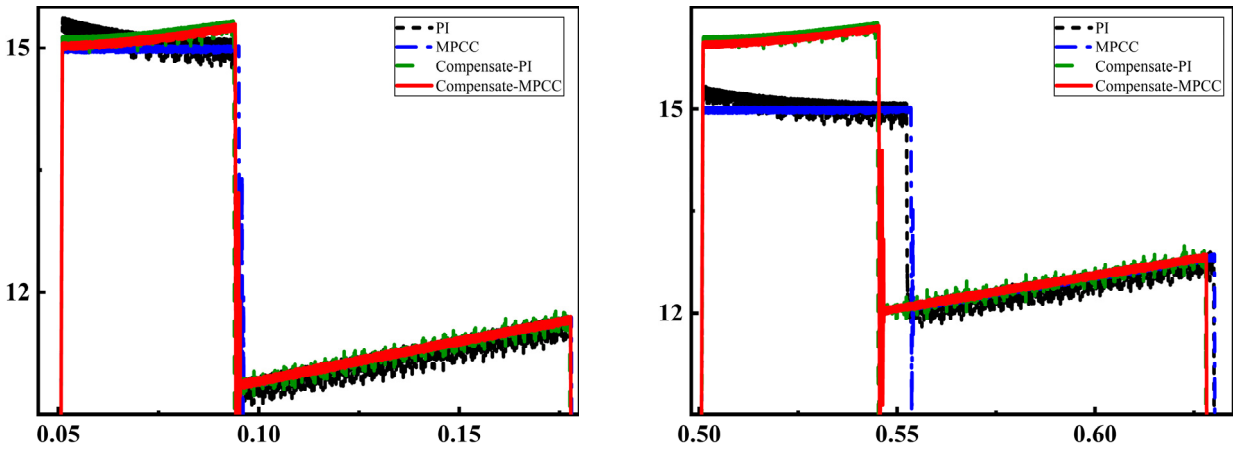

(**b**) (**c**)

Figure 11. Q-axis current graphs. (**a**) General curve of q-axis current. (**b**) Partial enlargement 1. (**c**) Partial enlargement 2.

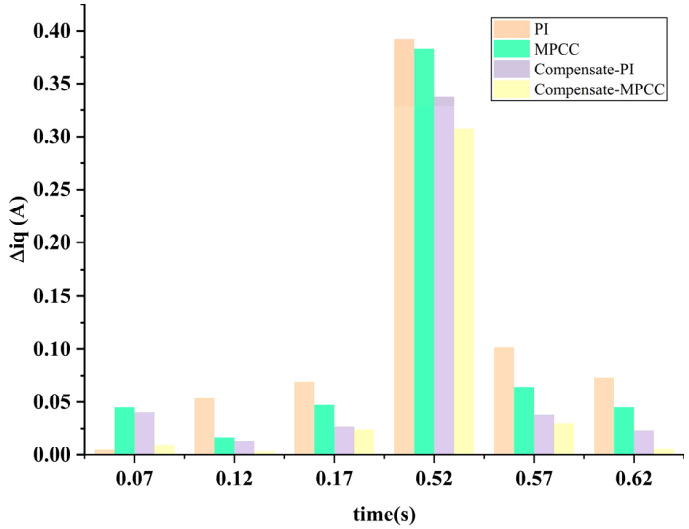

Figure 12. Fluctuation of q-axis current at different sampling times.

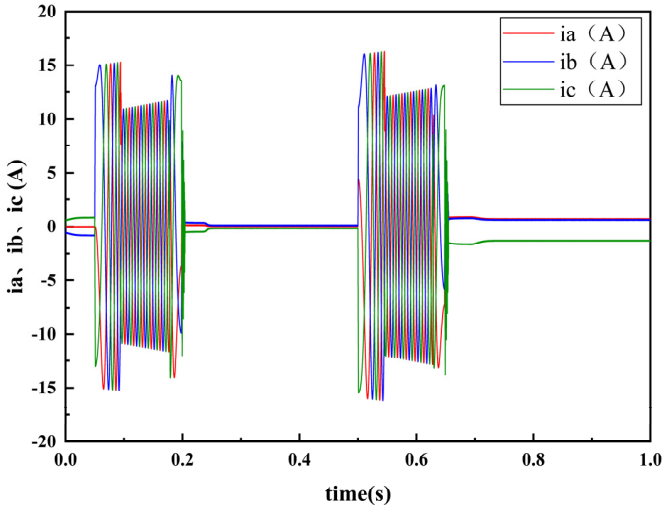

(**a**)

Figure 13. *Cont.*

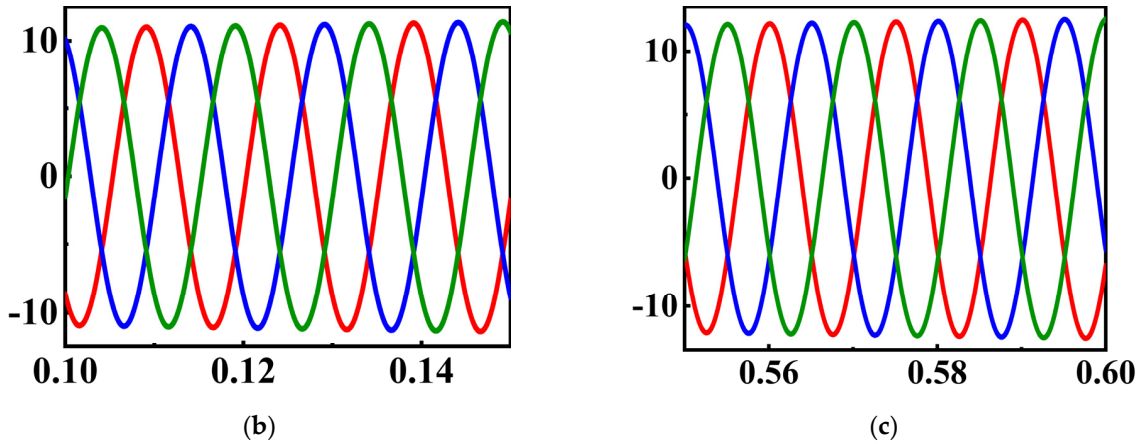

(**b**) (**c**)

Figure 13. Three-phase stator current curves under Compensate–MPCC control method. (**a**) General curve of stator three-phase current under Compensate–MPCC control method. (**b**) Partial enlargement 1. (**c**) Partial enlargement 2.

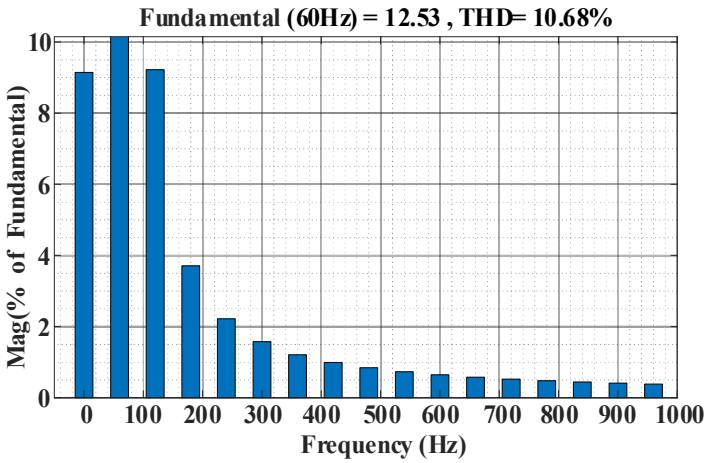

Figure 14. Harmonic analysis of three-phase stator current.

Table 4. Comparison of EMA output displacement results under different control methods.

Method of Control	Time	Reference Value	Actual Value	Time	Reference Value	Actual Value
Symbol/Unit	***t*/s**	**x_r/mm**	***x*/mm**	***t*/s**	**x_r/mm**	***x*/mm**
PI	0.2	50	49.812	0.66	100	99.864
MPCC			49.884			99.887
Compensate–PI	0.2	50	49.948	0.66	100	99.947
Compensate–MPCC			49.994			99.963

Table 5. Comparison of tracking error results under different control methods.

Method of Control	Time	Reference Value	Error Value	Time	Reference Value	Error Value
Symbol/Unit	***t*/s**	**x_{er}/mm**	**x_e/mm**	***t*/s**	**x_{er}/mm**	**x_e/mm**
PI	0.2	±0.1–±0.2	−0.144	0.66	±0.1–±0.2	−0.100
MPCC			−0.101			−0.087
Compensate–PI	0.2	±0.1–±0.2	−0.019	0.66	±0.1–±0.2	−0.031
Compensate–MPCC			−0.003			−0.026

Table 6. Comparison of speed results under different control methods.

Method of Control	Time	Reference Value	Actual Value	Time	Reference Value	Actual Value
Symbol/Unit	***t*/s**	**ω_r/r·min^{-1}**	**ω/r·min^{-1}**	***t*/s**	**ω_r/r·min^{-1}**	**ω/r·min^{-1}**
PI	0.095	1000	996.90	0.547	1000	950.55
MPCC			999.04			945.01
Compensate–PI			999.29			999.29
Compensate–MPCC			999.47			999.46

Table 7. Fluctuation of q-axis current at different sampling times.

Method of Control	Time	Standard Deviation	Time	Standard Deviation	Time	Standard Deviation
Symbol/Unit	***t*/s**		***t*/s**		***t*/s**	
PI	0.12	0.053	0.52	0.392	0.62	0.073
MPCC		0.016		0.383		0.045
Compensate–PI		0.013		0.337		0.023
Compensate–MPCC		0.003		0.307		0.005

Figure 7 shows the output displacement tracking curve of the flap EMA before and after compensation using the two control methods. In the simulation, the system was given an initial reference displacement of 50 mm at 0.05 s, corresponding to the scenario in Figure 1 where the flap is not fully lowered. The second reference displacement of 100 mm was given at 0.5 s, corresponding to the scenario in Figure 1 where the flap is fully lowered. As shown in Figure 7, both control methods, before and after compensation, were able to track the given position. A local zoom in Figure 7 shows the tracking performance near the reference position at 0.2 s, while another zoom focuses on performance near the position at 0.65 s. The figure indicates that the Compensate–MPCC control method tracks faster compared to the other methods. Table 4 presents a comparison of the output displacement results under different control methods. The localized zoomed-in graphs in Figure 7 indicate that the four control methods approach the first and second reference displacements at approximately 0.2 s and 0.66 s, respectively. Therefore, Table 4 was used to compare the flap EMA output displacement data at 0.2 s and 0.66 s in the simulation. Table 4 shows that the output displacement of the Compensate–MPCC control method is closer to the system's reference displacement compared to the other control methods.

Figure 8 presents the position tracking error curve, showing that the Compensate–MPCC control method has a smaller position tracking error compared to other control methods. Table 5 compares the tracking error results across different control methods. The control accuracy of the flap electromechanical actuator is generally required to be within a displacement range of ± 0.1 to ± 0.2 mm. As shown in Table 5, the errors for all methods fall within the required range; however, the Compensate–MPCC control method proposed in this paper achieves a smaller tracking error and higher accuracy compared to the other methods.

Figure 9 illustrates the PMSM speed curve, while Table 6 compares the speed results across different control methods. By combining Figures 7 and 9, it can be observed that during the two position tracking processes, both control methods, before and after compensation, quickly reached the vicinity of the rated speed, demonstrating a fast dynamic response. The two enlarged views, along with Table 6, show that the MPCC, Compensate–PI, and Compensate–MPCC methods exhibit relatively small speed tracking errors compared to the traditional PI control method, with the Compensate–MPCC method achieving the smallest speed tracking error. However, the traditional PI control method provides smoother speed operation when approaching the rated speed compared to the other control methods.

Figure 10 shows the electromagnetic torque curve. It can be observed that torque pulsation is larger with the traditional PI control method and smaller with the Compensate-

MPCC control method after gear backlash torque and friction torque current compensation. Based on the calculation and analysis of electromagnetic torque data, the Compensate-MPCC control method reduces torque ripple by 15.4% compared to the traditional PI control method.

Figure 11 shows the q-axis current curve. By calculating the mean and standard deviation of the q-axis current data at different sampling times, the q-axis current fluctuations during system operation are shown in Figure 12. Table 7 presents the q-axis current fluctuations at 0.12 s, 0.52 s, and 0.62 s under different control methods and sampling times. From the simulation results and data comparison, it is evident that the two control methods with gear backlash compensation and friction compensation result in smaller q-axis current fluctuations compared to the uncompensated control method. As shown in Figure 12 and Table 7, the Compensate–MPCC control method exhibits the smallest current fluctuation among the four control methods and demonstrates superior static characteristics. In contrast, the traditional PI control method shows the largest q-axis current fluctuation.

Figure 13 shows the three-phase stator current waveform under the Compensate–MPCC control method, and Figure 14 presents the harmonic analysis of the three-phase stator current. These figures show that the three-phase stator current waveform is slightly distorted during the system's start–stop process. However, when the system operates stably, the current waveform exhibits better sinusoidal characteristics. At this time, the total harmonic distortion (THD) of the current is 10.68%, indicating relatively stable overall performance.

5. Conclusions

This paper investigates the issues of gear backlash and nonlinear friction interference in the mechanical transmission system of a flap electromechanical actuator (EMA) and develops a comprehensive simulation model by analyzing its characteristics. The simplified gear backlash dead zone model and LuGre friction model are employed to create torque–current compensation models. The q-axis current is compensated and controlled through feedforward compensation, which enhances the position control accuracy of the system while reducing torque pulsation and current ripple during operation. A comparison of simulation results demonstrates that the proposed control method, which incorporates gear backlash and friction compensation, improves position tracking accuracy and reduces torque pulsation and q-axis current ripple compared to the traditional PI and MPCC control methods in the uncompensated case. In summary, the control method proposed in this paper effectively mitigates the impact of gear backlash and nonlinear friction on system control performance.

Author Contributions: Conceptualization, Q.Z. and H.D.; methodology, Q.Z. and H.D.; software, Q.Z.; validation, Q.Z.; investigation, Q.Z.; resources, Q.Z.; data curation, Q.Z.; writing—original draft preparation, Q.Z.; writing—review and editing, Q.Z. and H.D.; supervision, B.W., J.C. and H.D.; project administration; funding acquisition, B.W., J.C. and H.D. All authors have read and agreed to the published version of the manuscript.

Funding: This study was supported by the Major Science and Technology Program of Gansu Province, China (22ZD6GA027). Sponsor: Haiying Dong.

Data Availability Statement: The data that has been used are confidential.

Acknowledgments: The completion of this study is due to the collaborative efforts of several co-authors.

Conflicts of Interest: Bo Wang and Jingbo Chen were employed by the company Academy, Lanzhou Wanli Airlines Electromechanical Limited Liability Company. The remaining authors declare that this research was conducted in the absence of any commercial or financial relationships that could be construed as potential conflicts of interest.

References

1. Wang, Z.; Jiang, D.; Liu, Z.; Zhao, X.; Yang, G.; Liu, H. A Review of EMI Research of High Power Density Motor Drive Systems for Electric Actuator. *Actuators* **2023**, *12*, 411. [CrossRef]
2. Wu, Z.; Li, W.; Tang, H.; Luo, S.; Zhang, L. A review of control strategies for the full-domain high-efficiency operation of wide-speed permanent magnet synchronous motors. *Proc. CSEE* **2023**, *43*, 2496–2512. [CrossRef]
3. Yang, J.Z.; Li, Y.C.; Wang, F.; Diao, C. Nonlinear tracking controller design for flap electromechanical actuator. *Comput. Simul.* **2015**, *32*, 100–105. [CrossRef]
4. Gan, L.; Wang, L.; Huang, F. Adaptive Backlash Compensation for CNC Machining Applications. *Machines* **2023**, *11*, 193. [CrossRef]
5. Han, K.-H.; Koh, G.-O.; Sung, J.-M.; Kim, B.-S. An Adaptive Control Approach for Improving Control Systems with Unknown Backlash. *Int. J. Aeronaut. Space Sci.* **2011**, *12*, 360–364. [CrossRef]
6. Zhang, D.; Wang, Z.; Tomizuka, M. A variable-parameter-model-based feedforward compensation method for tracking control. *IEEE/CAA J. Autom. Sin.* **2020**, *7*, 693–701. [CrossRef]
7. Liu, H.; Li, S. Speed Control for PMSM Servo System Using Predictive Functional Control and Extended State Observer. *IEEE Trans. Ind. Electron.* **2012**, *59*, 1171–1183. [CrossRef]
8. Bolognani, S.; Peretti, L.; Zigliotto, M. Design and Implementation of Model Predictive Control for Electrical Motor Drives. *IEEE Trans. Ind. Electron.* **2009**, *56*, 1925–1936. [CrossRef]
9. Yu, Z.; Wang, L.; Su, J. Uncertain linear multivariable system control based on disturbance observer. *Acta Autom. Sin.* **2014**, *40*, 2643–2649.
10. Que, N.; Deng, W.; Zhou, N.; Yao, J. Disturbance Observer Based Prescribed-Time Tracking Control of Nonlinear Systems with Non-Vanishing Uncertainties. In *IEEE Transactions on Circuits and Systems II: Express Briefs*; IEEE: Piscataway, NJ, USA, 2024; Volume 71, pp. 3131–3135. [CrossRef]
11. Li, B.; Chen, X.; Lin, H.; Lv, S.; Ma, D. Backlash compensation and terminal sliding mode control of electromechanical servo system. *Trans. China Electrotech. Soc.* **2016**, *31*, 162–168. [CrossRef]
12. Guo, J.; Yao, B.; Wu, Y.; Chen, W. Adaptive robust control of a class of nonlinear uncertain systems with input gaps. *Control Decis.* **2010**, *25*, 1580–1584.
13. Li, Z.; Zhai, J. Fuzzy Adaptive Super-Twisting Sliding Mode Asymptotic Tracking Control of Robotic Manipulators. *Int. J. Fuzzy Syst.* **2023**, *26*, 34–43. [CrossRef]
14. Wang, H.; Chen, B.; Liu, K.; Liu, X.; Lin, C. Adaptive Neural Tracking Control for a Class of Nonstrict-Feedback Stochastic Nonlinear Systems with Unknown Backlash-Like Hysteresis. *IEEE Trans. Neural Netw. Learn. Syst.* **2014**, *25*, 947–958. [CrossRef] [PubMed]
15. Lv, C.; Wang, B.; Chen, J.; Zhang, R.; Dong, H.; Wan, S. Research on a Torque Ripple Suppression Method of Fuzzy Active Disturbance Rejection Control for a Permanent Magnet Synchronous Motor. *Electronics* **2024**, *13*, 1280. [CrossRef]
16. Zheng, N. Self-immunity control strategy for dual motor-driven servo system. *Comput. Simul.* **2017**, *34*, 376–380. [CrossRef]
17. Wan, S.; Wang, B.; Chen, J.; Dong, H.; Lv, C. Model Predictive Control Strategy Based on Loss Equalization for Three-Level ANPC Inverters. *Actuators* **2024**, *13*, 111. [CrossRef]
18. Gao, B.; Shen, W.; Zheng, L.; Zhang, W.; Zhao, H. A Review of Key Technologies for Friction Nonlinearity in an Electro-Hydraulic Servo System. *Machines* **2022**, *10*, 568. [CrossRef]
19. Zhang, T.; Li, X.; Gai, H.; Zhu, Y.; Cheng, X. Integrated Controller Design and Application for CNC Machine Tool Servo Systems Based on Model Reference Adaptive Control and Adaptive Sliding Mode Control. *Sensors* **2023**, *23*, 9755. [CrossRef]
20. Hu, Y.; Zhu, T.; Jiang, P.; Liu, F.; Chen, Y. Research on road friction compensation of steering-by-wire system. *J. Hefei Univ. Technol. (Nat. Sci.)* **2020**, *43*, 584–589+595.
21. Han, X.; Dong, H.; Wang, M.; Jin, J.; Dong, Q.; Zhang, L. Compensation method of Stribeck friction moment in optically stabilised platform. *Fire Control Command Control* **2019**, *44*, 123–126.
22. Jiang, C.; Dong, X.; Jin, L.; Lu, D. Modelling and analysis of contact friction characteristics of radial standing wave ultrasonic motors. *Proc. CSEE* **2021**, *41*, 6081–6090. [CrossRef]
23. Xie, L.; Liu, L.; Zheng, X.; Wang, X. Sliding mode control of aircraft braking system based on LuGre model. *J. Huazhong Univ. Sci. Technol. (Nat. Sci. Ed.)* **2013**, *41*, 65–69.
24. Huang, D.; Yang, J.; Xu, G.; Chen, J. LuGre-Net: A hybrid neural network for friction modeling of feed systems in machine tools. *Nonlinear Dyn.* **2024**, *12*, 11927–11943. [CrossRef]
25. Xi, T.; Fujita, T.; Kehne, S.; Ikeda, R.; Fey, M.; Brecher, C. An Extended LuGre Model for Estimating Nonlinear Frictions in Feed Drive Systems of Machine Tools. *Procedia CIRP* **2022**, *107*, 452–457. [CrossRef]
26. Soleimanian, P.; Ahmadian, H. Modeling Friction Effects in Lubricated Roller Guideways Using a Modified LuGre Model. *J. Vib. Control* **2021**, *28*, 2519–2530. [CrossRef]
27. Liu, C.; Luo, G.; Tu, W. A review on the self-immunity control of aero-mechanical actuated permanent magnet synchronous motors. *J. Electr. Eng.* **2021**, *16*, 12–24.
28. Zhao, C.; Zhou, J.; Li, X. EMA three-closed-loop servo control system based on permanent magnet synchronous motor. *J. Chongqing Univ. Technol. (Nat. Sci.)* **2016**, *30*, 104–111.

29. Sun, J. Research on Friction Compensation and Application of High Frequency Responsive Direct Drive Valve. Master's Thesis, Shandong University, Shandong, China, 2020. [CrossRef]
30. Liu, X.; Xie, M. Friction Compensation Control Strategy for Electric Servo System of Aircraft Servos. *Modul. Mach. Tool Autom. Manuf. Technol.* **2022**, *5*, 45–50. [CrossRef]
31. Shen, D. Research on Modeling, Analysis and Nonlinear Control Method in Electromechanical Operating System. Master's Thesis, Southeast University, Nanjing, China, 2018.